American Mineralogist, Volume 88, pages 1560–1574, 2003

Phase transformations and reaction kinetics during the temperature-induced oxidation of natural olivine

ALESSANDRO F. GUALTIERI,[1,*] MAURO GEMMI,[2] AND MONICA DAPIAGGI[2]

[1]Dipartimento di Scienze della Terra, Università di Modena e Reggio Emilia I-41100 Modena, Italy
[2]Dipartimento di Scienze della Terra "Ardito Desio", Università di Milano I-20133 Milano, Italy

ABSTRACT

This work describes the sequence of transformations and their reaction kinetics during the oxidation of olivine in air at high temperature. A natural olivine sample from the layered series of the Ivrea-Verbano igneous complex (Western Alps, Italy) was heated in the temperature range 25–1300 °C in air and investigated by in situ, real time powder X-ray diffraction (PXRD). The evolution of the peaks (measured integrated intensities) was followed in non-isothermal conditions using variable heating rates (b = 20, 22, 25, 27, and 30 °C/min). The total time of the experiments ranged from about 256 (b = 30 °C/min) to 277 (b = 20 °C/min) min including the time for the data collections. An additional isothermal run was performed at 800 °C. The analysis of the kinetic data was attempted with the use of different equations including the classical Avrami theory for solid-state reactions. The kinetic results were confirmed by independent experimental data from electron microscopy (SEM, TEM).

In the transformation sequence, hematite appears at about 600 °C producing amorphous segregations. of silica that later recombine with forsterite to form pyroxene Hematite is stable up to 1130 °C where it is transformed into magnetite. The rate limiting step for the formation of hematite is a two-dimensional diffusion with constant or decelerating nucleation rate and apparent activation energy of 15 kcal/mol. The concentration of Fe^{3+} in Fe-rich regions favors the heterogeneous nucleation of hematite, which may take place on existing defects or at the grain boundaries with impurity phases such as serpentine. At 1130 °C, magnetite is formed at the expenses of hematite, with a contracting volume interface-controlled reaction in two or three dimensions with an apparent activation energy of 30–31 kcal/mol. The hematite to magnetite transformation is direct, without a metastable amorphous intermediate. It is described by the "shrinking core model," with the formation of a magnetite outer layer at the surface of the hematite particles that proceeds toward the core of the reacting hematite by diffusion of the oxygen throughout the newly formed magnetite layer. Its rate is limited by the advancement of the reaction front. The rate-limiting step for the formation of pyroxene is two-dimensional diffusion with decelerating nucleation rate with an apparent activation energy of 29 kcal/mol.

INTRODUCTION

Olivine is an orthosilicate (space group *Pbnm*) composed of isolated $[SiO_4]^{4-}$ tetrahedra connected via divalent cations in sixfold coordination. The O atoms lie in sheets parallel to the (100) plane in an approximately hexagonal close packing. Silicon-centered tetrahedra point alternately up and down along the **a** and **b** axes. Divalent cations occupy two distinct octahedral sites; M1 located on centers of symmetry and M2 located on mirror planes. The M1 octahedra share six of twelve edges with other polyhedra: two with other M1 octahedra, two with M2 octahedra, and two with tetrahedra. The M2 octahedra share only three edges: two with M1 octahedra and one with a tetrahedron (Deer et al. 1962). Natural olivines are generally intermediate terms between the end-members forsterite (Fo_{100}, Mg_2SiO_4) and fayalite (Fa_{100}, Fe_2SiO_4), with minor replacement by Mn and Ca, especially in the Fe-rich members. The distribution of cations in the M1 and M2 sites has been studied using different methods: X-ray diffraction (Finger 1970; Brown and Prewitt 1973; Smyth and Hazen 1973; Hazen 1976; Will and Nover 1979; Nobuyuki et al. 1985; Princivalle 1990; Ottonello et al. 1990; Artioli et al. 1993); neutron diffraction (Caron et al. 1965; Newnham et al. 1966; Redfern et al. 1997); Mössbauer spectroscopy (Bancroft et al. 1967; Bush et al. 1970); EPR spectroscopy (Weeks et al. 1974); absorption spectroscopy (Brown 1970; Scheetz and White 1972; Wood 1974); and vibrational spectroscopy (Duke and Stephens 1964; Huggins 1973). A comprehensive list of the olivine structure types is found in Brown (1980).

The oxidation of olivine is of great petrologic interest because olivine is the most common igneous rock-forming Fe-Mg silicate mineral and for its buffering properties (Khisina et al. 1995). A short description of the results of the laboratory oxidation experiments of olivine is given first, followed by a summary of the results of naturally oxidized olivine samples.

Olivine is thermodynamically stable only within a limited range of oxygen fugacity. Under oxidizing conditions, a change in stoichiometry occurs and Fe^{2+}, Fe^{3+}, and physically dissolved O atoms are in equilibrium (i.e., $4Fe^{3+} + 2O^{2-} \rightarrow 4Fe^{2+} + O_2$). Metastable olivine transforms into Fe^{3+}-rich phases and silica-rich phases depending on temperature, oxygen fugacity, Fe

* E-mail: alex@unimore.it

content, and reaction kinetics (Putnis 1979).

An early study of the oxidation reactions of Fa_{53} olivine (Koltermann 1962) showed that: (1) a fast heating rate to 820 °C leads to the formation of forsterite + amorphous silica + hematite; (2) a fast heating rate to 1080 °C leads to the formation of forsterite + cristobalite + hematite + enstatite; and (3) a slow heating rate to 1100 °C leads to the formation of forsterite + amorphous silica + magnetite. Fisler et al. (1997) confirmed the presence of enstatite in the reaction series and showed that its growth increases with temperature according to a parabolic law controlled by ionic diffusion.

Champness (1970) studied the oxidation of olivine over the temperature range 500–800 °C, and observed that hematite, magnetite, and amorphous silica were formed along linear defects of olivine. Hematite and magnetite invariably showed the same topotactic relationship with olivine, with the growth direction determined by the orientation of the dislocations that formed in the olivine matrix.

The kinetics of the oxidation of Fa_{11} olivine with an average grain size of 70 μm were investigated at 600 °C (Khisina et al. 1998) and 700 °C (Khisina et al. 1995). These studies revealed the earlier nucleation of laihunite inside the planar defects of olivine. Laihunite [$(Mg_{0.5}\square_{0.5}Fe^{3+})SiO_4$] is an intermediate member of the polysomatic series olivine $(Me^{2+})SiO_4$-ferriolivine $(Fe^{3+})(Me^{2+})_{0.5}\square_{0.5}SiO_4$, where □ are the vacancies in the M1 site and Me are divalent cations such as Mg^{2+}, Ni^{2+}, Co^{2+}, Mn^{2+}, and Fe^{2+} (Veblen 1991). Laihunite has a monoclinic superstructure with Fe^{3+} in M2 and (Fe^{2+}, □) in M1. Magnesioferrite forms in the internal oxidation layers within the laihunite sheets. According to Khisina et al. (1998), the rate-limiting step of the laihunite formation is the reaction interface, whereas the rate-limiting step of the magnesioferrite reaction is diffusion. The reaction enthalpies were 17 kcal/mol and 28 kcal/mol, respectively. According to Wu and Kohlsted (1988) and Mackwell (1992), the diffusion rate of the O and Si species in olivine is much slower than the diffusion rate of Mg and Fe, indicating that the diffusion reaction concerns only Fe and Mg (and vacancies).

Using Rutherford spectroscopy, Wu and Kohlsted (1988) investigated the oxidation of an olivine with composition Fa_5 in the range 700–1100 °C for variable times (0.5–100 h), and found that olivine grains invariably show an internal oxidation layer with magnetite and amorphous silica, and an external oxidation layer with MgO and $MgFe_2O_4$ but no silica. The reaction kinetics are limited by ion diffusion, which takes place throughout the crystal lattice for Mg (with an activation energy of about 33 kcal/mol) and along the linear defects for Fe (with activation an energy of about 45 kcal/mol). A similar experiment was attempted by Khisina et al. (2000) on an olivine grain (15 mm diameter) from 9206 Udachnaya kimberlite heated at 700 °C for 9 h in air at 1 atm. These authors found a layered microstructure characterized by Mg-enriched secondary olivine at the outer layers, and Fe-enriched phases in the core layers with metastable phases such as feroxyhyte, bernalite, and β-cristobalite. The thermodynamically stable products under oxidizing conditions are magnetite, hematite, and quartz, whereas heating olivine powder under the same P-T-PO_2-t conditions would have resulted in the formation of laihunite + magnesioferrite + quartz for longer times (Khisina et al. 1995).

Recently, $Fa_{100} - Fa_{70}$ olivines were oxidized in alkaline and acidic aqueous environments (Iishi et al. 1997). In alkaline environment, laihunite, and hematite precipitated along the (100) and (001) olivine planes, whereas in the acidic environment, amorphous silica and hematite precipitated along the (001) olivine planes.

For naturally oxidized olivines, Putnis (1979) described the mechanism by which the microstructure was developed during the oxidation of olivines from the ultrabasic layered intrusion of Rhum, Inner Hebrides. Two sets of platelets were observed on the {101} planes of olivine. Most of the platelets consist of clinopyroxene and contain rounded inclusions of magnetite at approximately regular intervals along the length of the platelet. The orientation of pyroxene and included magnetite relative to the olivine matrix appears to be completely arbitrary whereas individual magnetite regions have the same orientation. The overall pyroxene-magnetite intergrowth suggests a simultaneous nucleation of the two phases from a single precursor, and their morphology and orientation relations have many characteristics of the eutectoid decomposition of the precursor phase by a cellular precipitation mechanism.

Dyar et al. (1998) used synchrotron micro-XANES spectroscopy to investigate five natural fayalite samples including one from Qianan (China) that was almost completely oxidized and contained a fine intergrowth of silica, laihunite, and hematite. Similarly, Puga et al. (1999) investigated inclusions of magnetite and other silicates in an igneous olivine from metagabbroic rocks of the Betis Ophiolitic Association (BOA, Mulhaćen Complex, Spain). They found that magnetite precipitates display a fixed orientation relative to the olivine host, and form intergrowths with monoclinic amphibole, orthorhombic amphibole, and monoclinic pyroxene.

Mikouchi et al. (2000) studied oxidized olivine in the martian meteorite Nakhla, and found that all the crystals invariably contain 2–3 μm long black lamellar inclusions of augite and magnetite. These inclusions are probably very similar to those called "symplectite," and were formed by exsolution (Moseley 1984) at $T > 900$ °C during cooling.

The above review of the literature reveals a confused scenario and the lack of a clear and comprehensive picture of the reaction sequence and related kinetics of phase transformations during the oxidation of olivine over a range in temperature. A reason may be that only a handful of studies have dealt with the kinetics of the oxidation reaction: (1) Mackwell (1992) by direct observation of the formation of oxidation layer on the external surface of fayalite in air; (2) Khisina et al. (1995) using combined TEM and Mössbauer spectroscopy in air at 600 °C; (3) Khisina et al. (1995, 1998) in air at 350–700 °C using combined TEM and Mössbauer spectroscopy. In the present study, a natural olivine sample from the Western Alps (Italy) was heated in the temperature range 25–1300 °C in air. The complete sequence of phase transformations and reaction kinetics was investigated in situ by real time powder X-ray diffraction (PXRD). The kinetic study was complemented by observations of the evolution of the system at a meso- and micro-scale by electron microscopy (SEM, TEM).

EXPERIMENTAL METHODS AND KINETIC ANALYSIS

Sample selection and characterization

A natural olivine sample from the layered series of the Ivrea-Verbano igneous complex (Western Alps, Italy) was investigated. Its occurrence was described elsewhere (Rivalenti et al. 1984). The chemical composition (m wt% oxide) of the olivine crystals obtained by microprobe analysis is: SiO_2 = 39.52, Al_2O_3 = 0.0, TiO_2 = 0.0, FeO = 16.10, MnO = 0.22, MgO = 43.82, CaO = 0.0, Na_2O = 0.0, K_2O = 0.0, P_2O_5 = 0.0, Sum = 99.66 (Rivalenti et al. 1984). The water content, determined from the TG analysis, is 0.5 wt%. The original rock sample was crushed, sieved to an average grain size of less than 2 mm, and then sonicated to separate grain aggregates. After the preliminary preparation, olivine crystals were selected manually and separated from the matrix using optical microscopy.

To obtain an accurate quantitative phase analysis and structural data of the olivine sample at room temperature, a Rietveld refinement was performed. The sample was hand ground in an agate mortar to reach a maximum diameter of about 20–30 μm for the particle aggregates (according to laser diffraction). The powder was side-loaded in an aluminum flat holder, and the X-ray data were collected using a Philips conventional Bragg-Brentano vertical diffractometer with Cu$K\alpha$ radiation and a secondary pyrolitic graphite crystal monochromator. The investigated 2θ range was 5–80° with steps of 0.02° and 15 s per step. Observed data were refined with GSAS (Larson and Von Dreele 1994).

In situ PXRD and kinetic analysis

The data set for the kinetic analysis was collected using a Philips X'Pert PW 3701 powder diffractometer in parafocusing Bragg-Brentano vertical θ-θ geometry. The experimental setup is characterized by a divergent 0.5° slit on the secondary graphite-monochromatized beam (Cu$K\alpha$ radiation) and a receiving 0.1 mm slit on the diffracted beam. The diffractometer is equipped with a PAP 1600 hot chamber (Dapiaggi et al. 2002). The temperature stability is assured by two alumina fiber blocks heated by two $MoSi_2$ resistances and the sample holder is composed of a dense alumina disk placed over a cold finger. The sample can be rotated for better temperature homogeneity and higher counting statistics. The data were collected in air with an angular step size of 0.02° and 0.5 s/step. The time-resolved runs for the kinetic analysis were performed in the range 29–45 °2θ, where intense and well-defined peaks of the investigated phases are shown. The total time for collection of each data set is about 6.5 min, a good compromise to obtain a sufficient counting statistics and to prevent the sample from reacting during that time.

The evolution of the peaks (measured integrated intensities) was followed in non-isothermal conditions using variable heating rates (b = 20, 22, 25, 27, and 30 °C/min). The total time of the experiments ranged from about 256 (b = 30 °C/min) to 277 (b = 20 °C/min) min, which includes the time for data collection. Data were collected in steps of 25 °C from 600 to 1300 °C. An additional isothermal run was performed at 800 °C with b = 30 °C/min to reach the isothermal temperature. A preliminary analysis of the slow run with b = 20 °C/min showed that the newly formed phases were in sequence hematite, pyroxene, and magnetite. To get an accurate quantitative phase analysis of the sample at high temperature, a Rietveld refinement was performed on the data collected in situ of the olivine sample fired at 1270 °C with b = 20 °C/min.

For the patterns of each run, the integrated intensity of the diffraction peaks of olivine (the $\bar{1}$31, 131, and 221 peaks), hematite (the 104 and 113 peaks), pyroxene (the $\bar{2}$21 and 310 peaks), and magnetite (the 400 and 222 peaks) was extracted by means of the Simpsons method and the background was subtracted using a linear interpolation. For the isothermal run at 800 °C, collected to compare the kinetic parameters calculated with the non-isothermal method, only the integrated intensity of the diffraction peaks of olivine (the 031, 131, and 221 peaks) was extracted. The integrated intensities were normalized and plotted as α-time curves for the kinetic analysis.

Kinetic analysis

The rate of a kinetic process can be expressed as:

$$\frac{d\alpha}{dt} = kf(\alpha) \tag{1}$$

or in the integral form

$$g(\alpha) = kt \tag{2}$$

where α is the conversion factor, k is the rate constant with respect to time t, $f(\alpha)$ is the kinetic model function that depends on the mechanism of the reaction and, $g(\alpha)$ is the integral of $\frac{1}{f(\alpha)}$. The reaction rate is temperature dependent and is assumed to follow the Arrhenius equation:

$$k = Ae^{\left(-\frac{E}{RT}\right)} \tag{3}$$

where T is the absolute temperature, R is the molar gas constant, E is the apparent activation energy, and A is the frequency factor. Non-isothermal experiments are performed using a constant heating rate. An expression that forms the basis of non-isothermal data analysis can be derived by combining the rate Equation 1 with the Arrhenius Equation 3, assuming a constant heating rate, integrating, and substituting $X = \frac{E}{RT}$:

$$g(\alpha) = -\frac{AE}{Rb}\int_{X0}^{X} e^{-X}X^{-2}dX \tag{4}$$

where

$$p(X) = \int_{X0}^{X} e^{-X}X^{-2}dX \tag{5}$$

In the literature, $p(X)$ is called "the temperature integral" and cannot be integrated. A member of approximating formulas for $p(X)$ have been proposed and are in common use (e.g., Murray and White 1955).

The kinetic model for nucleation and crystal growth in solids, formulated by Avrami (Bamford and Tipper 1980), has the following general formulation is:

$$\alpha = 1 - e^{\left[-(kt)^n\right]} \tag{6}$$

The value of n depends on the mechanism and dimensionality of nucleation and growth. For interface-controlled growth, n is an integer, and for diffusion-controlled growth, n takes either integer or half-integer values. Differentiating Equation 6 with respect to time gives:

$$\frac{d\alpha}{dt} = kn(1-\alpha)\left[-\ln(1-\alpha)\right]^{1-\frac{1}{n}} \tag{7}$$

which is referred to as the Johnson-Mehl-Avrami (JMA) equation, developed for the interpretation of isothermal data. The validity of the JMA equation can be extended to non-isothermal conditions (Henderson 1979).

Four methods of non-isothermal kinetic analysis have been used here. Because each method requires one or more assumptions, a cross check of the results was attempted. The method of Coats and Redfern (1964) was used to calculate the kinetic parameters A and E assuming a kinetic expression. The method of Kennedy and Clark (1997) was used to calculate A and E assuming a kinetic expression and the temperature at which the reaction starts. The Kissinger method (Bamford and Tipper 1980) permits the calculation of E assuming the peak temperature of the corresponding DTA reaction peak. The direct application of the general expression of the Avrami-Erofe'ev

equation (Bamford and Tipper 1980) permits the determination of n, related to the reaction mechanism, assuming the relative value of E. The Avrami-Erofe'ev equation also has been applied to the isothermal data.

The method developed by Coats and Redfern (1964) is based on the equation:

$$\ln g(\alpha) - 2\ln T \cong \ln\left[\frac{AR}{Eb}\right] - \frac{E}{RT} \quad (8)$$

The kinetic parameters A and E are determined using several kinetic expressions whose integral form is reported in Table 1.

The method proposed by Kennedy and Clark (1997) is based on the expression:

$$T = bt + T_0 \quad (9)$$

where T_0 is the temperature at the start of the reaction. The basic equation is

$$\frac{bg(\alpha)}{(T - T_0)} = Ae^{-\frac{E}{RT}} \quad (10)$$

and taking the logarithm of both sides of this equation gives:

$$\ln\left[\frac{bg(\alpha)}{(T - T_0)}\right] = \ln(A) - \frac{E}{RT} \quad (11)$$

Plotting the left-hand side of this equation against $1/T$ should give a straight line of gradient –E/R and intercept ln(A), assuming the kinetic expressions $g(\alpha)$ reported in Table 1. T_0 is the temperature at which the reaction starts. The experimentally determined values are: T_0 = 873 K for the growth of hematite, T_0 = 1453 K for the growth magnetite, and T_0 = 1403 K for the growth of pyroxene.

The Kissinger equation (Bamford and Tipper 1980) is based on this expression:

$$\ln\left(\frac{b}{T_p^2}\right) = -\frac{E_c}{RT_p} + \text{constant} \quad (12)$$

where T_P is the peak temperature of the DTA reaction (endothermic and exothermic) peak. A plot of the left-hand side of the equation vs. $1/T_P$ is a line whose slope corresponds to E_C/R.

The direct application of the JMA equation to non-isothermal conditions for the calculation of the reaction order coefficient n requires the assumption of an apparent activation energy.

TABLE 1. The various available kinetic equations in the integral form

Rate controlling mechanism	kt =
P1 power law	$\alpha^{1/n}$
E1 exponential law	$\ln\alpha$
A2 Avrami-Erofe'ev 1	$[-\ln(1-\alpha)^{1/2}]$
A3 Avrami-Erofe'ev 2	$[-\ln(1-\alpha)^{1/3}]$
A4 Avrami-Erofe'ev 3	$[-\ln(1-\alpha)^{1/4}]$
B1 Prout-Tompkins	$\ln[\alpha/(1-\alpha)]$
R2 contracting area	$1-(1-\alpha)^{1/2}$
R3 contracting volume	$1-(1-\alpha)^{1/3}$
D1 one dimensional diffusion	α^2
D2 two dimensional diffusion	$(\alpha)\ln(1-\alpha)+\alpha$
D3 three dimensional diffusion Jander	$[1-(1-\alpha)^{1/3}]^2$
D4 Ginstling-Brounstein diffusion	$(1-2\alpha/3)-(1-\alpha)^{2/3}$
F1 first order	$-\ln(1-\alpha)$
F2 second order	$1/(1-\alpha)$
F3 third order	$[1/(1-\alpha)]^2$

The general expression of the Avrami-Erofe'ev equation (Bamford and Tipper 1980) is

$$[-\ln(1-\alpha)]^{1/n} = kt \quad (13)$$

The logarithmic transform of this equation was used to build a graph of ln[–ln(1–α)] vs. ln(t) in which isothermal experimental data are made linear in the so-called *ln-ln plot*. The reaction order (n) is calculated from the slope of the regression line whereas k, the rate coefficient, is calculated from the intercept. The experimental determination of the reaction order is a fundamental step for the interpretation of the reaction mechanism. For non isothermal data, the expression becomes:

$$[-\ln(1-\alpha)]^{1/n} = Ae^{(-\frac{Ea}{RT})(\frac{T}{b})\pi(\frac{Ea}{RT})} \quad (14)$$

where as E_a is the apparent activation energy, and $\pi(Ea/RT)$ is an approximation of the temperature integral. Although this method is very popular for isothermal experiments, the JMA model cannot always be applied to non-isothermal conditions. In fact, a double log function is not very sensitive to subtle changes in its argument, and this is even more likely under non-isothermal conditions where a similar double logarithmic plot vs. the reciprocal T is used. To test the applicability of the JMA model to non-isothermal data, Malek and Mitsuhashi (2000) proposed a test method based on the comparison of y(α) and z(α) plots of the isothermal and non-isothermal data with:

$$y(\alpha)_{iso} = k\cdot n(1-\alpha)[-\ln(1-\alpha)]^{1-1/n} \quad (15)$$
$$z(\alpha)_{iso} = n(1-\alpha)[-\ln(1-\alpha)] \quad (16)$$
$$y(\alpha)_{non\text{-}iso} = A\cdot n(1-\alpha)[-\ln(1-\alpha)]^{1-1/n} \quad (17)$$
$$z(\alpha)_{non\text{-}iso} = C\cdot n(1-\alpha)[-\ln(1-\alpha)] \quad (18)$$

with A = frequency factor, and $C = (b\cdot E_a/R)$. If such plots match, the JMA model can be utilized successfully for the data analysis we have verified the applicability of the JMA model using the test proposed by Malek and Mitsuhashi (2000) to the crystallization of hematite. For this reason, the isothermal curve collected at 800 °C was analyzed using the double log form of the classical JMA Equation 13 and the kinetic parameters used for the test.

Ex situ heating treatments

To investigate the evolution of the meso- and microstructure of olivine with temperature by electron microscopy (SEM and TEM, not yet in situ techniques at very high temperature), grains of the original sample were heated in a Lenton UAF 17/4 furnace with constant b = 20 °C/min at various temperatures (600, 700, 800, 900, 1000, 1100, 1200, and 1300 °C) and quenched in air.

Thermal analysis

Thermal analyses (TG, DTA) of the olivine powder were carried out in air using a Seiko TG/DTA 6300 instrument and b = 20 °C/min up to 1100 °C.

Electron microscopy

SEM (secondary and back-scattered electrons) observations were possible using a Philips XL40/604 at ca. 10^{-6} torr and a

variable tension of 10–25 kV. Single grains of the heated samples were encapsulated in an epoxy resin, coated with a thin gold layer of 10 nm, and polished to achieve smooth surfaces for the observation of the crystal morphology and phase relationships.

The samples for the TEM analysis were prepared by mild grinding of the original powder, followed by suspension in isopropyl alcohol and deposition on a holey carbon film grid. The TEM observation were carried out on three different instruments: a JEOL 2000 FX operating at 200 kV; a JEOL JEM 2010 operating at 200 kV equipped with a Link energy dispersive X-ray spectrometer and a Gatan energy filter; and a FEI/Philips Tecnai F20/ST with a field-emission gun also operating at 200 kV and equipped with an EDAX energy dispersive X-ray spectrometer and a Gatan Slow Scan CCD camera. All the micrographs presented here were recorded using CCD camera devices except those of magnetite, which were digitized from photographic plates using a Kite 12-bits CCD camera. The image enhancement was carried out using the program CRISP (Hovmöller 1992) and the image simulation was calculated using the multislice routines of the program JEMS.

RESULTS

The final agreement factors of the Rietveld refinement of the investigated olivine sample at room temperature are R_{wp} = 11.5%, R_p = 14.3%, and χ^2 = 5.0. The observed pattern, the calculated pattern, and difference curve are reported in Figure 1a. The results of the refinement reported in Table 2 reveal serpentine as an impurity in the olivine and the presence of less than 1 wt% spinel. The refined chemical composition of the olivine sample is Fa_{16}.

The final agreement factors of the Rietveld refinement of the sample at 1270 °C are R_{wp} = 10.4%, R_p = 12.9%, and χ^2 = 3.2. The observed pattern, the calculated pattern and difference curve are reported in Figure 1b. The results of the refinement, also reported in Table 2, show the presence of residual forsterite and a Cr-Fe spinel (<1 wt%) whose chemical composition was confirmed by spot energy dispersive analysis (EDS). The newly formed phases are hematite, magnetite, and proto-enstatite. Refinements using the ortho-enstatite and clino-enstatite models gave slightly higher agreement factors, indicating that proto-enstatite is presumably the phase observed here as indicated by the TEM results. The refined lattice parameters of these phases are: (1) forsterite: a = 4.8143(9), b = 10.400(1), c = 6.086(1) Å, V = 304.7(7) Å^3; (2) magnetite: a = 8.287(2) Å, V = 569.2(8) Å^3; (3) proto-enstatite with space group *Pbcn*: a = 9.31(1), b = 8.80(1), c = 5.34(1) Å, V = 443.5(9) Å^3; (4) hematite: a = 4.984(6), c = 14.33(2) Å, V = 308.5 Å^3; and (5) Cr-Fe spinel: a = 8.510(1) Å, V = 616.3(7) Å^3.

The reaction sequence observed by in situ PXRD shows hematite first, at about 600 °C, followed by proto-enstatite at about 1040 °C. Magnetite crystallizes from hematite at about 1130 °C. Figure 2a–2e depicts the α-temperature plots of the various non-isothermal runs relative to the growth and subsequent decomposition of hematite, growth of magnetite, and growth of pyroxene.

Table 3 reports the result of the best-fit analysis using the methods of Coats and Redfern (1964) (CR) and Kennedy and Clark (1997) (KC). A list of the tested kinetic functions appears in Table 1; only the results of the fitting procedure with $r^2 > 0.95$ are reported. In addition to calculated values of the apparent activation energies, the best-fit procedure gives an indication on the reaction mechanism of the four investigated reaction processes (growth and subsequent decomposition of hematite, growth of magnetite, and growth of pyroxene). It is well known, however, that these non-isothermal methods are quite insensitive to the reaction mechanism. In fact, only a preliminary indication of the reaction mechanism can be inferred from the CR and KC methods. Because of this limitation, other methods have been applied to elucidate better the reaction mechanism. The Kissinger method, in particular, permits the calculation of the apparent activation energy without any assumption of the reaction mechanism. Figures 3a–3d are logarithmic plots calculated using the Kissinger method (Bamford and Tipper 1980) with the relative apparent activation energies listed in Table 4. The resultant values of apparent activation energies were compared with those obtained with the CR and KC methods to assign the most probable reaction mechanism. In addition, Table 5 lists the results obtained by applying the

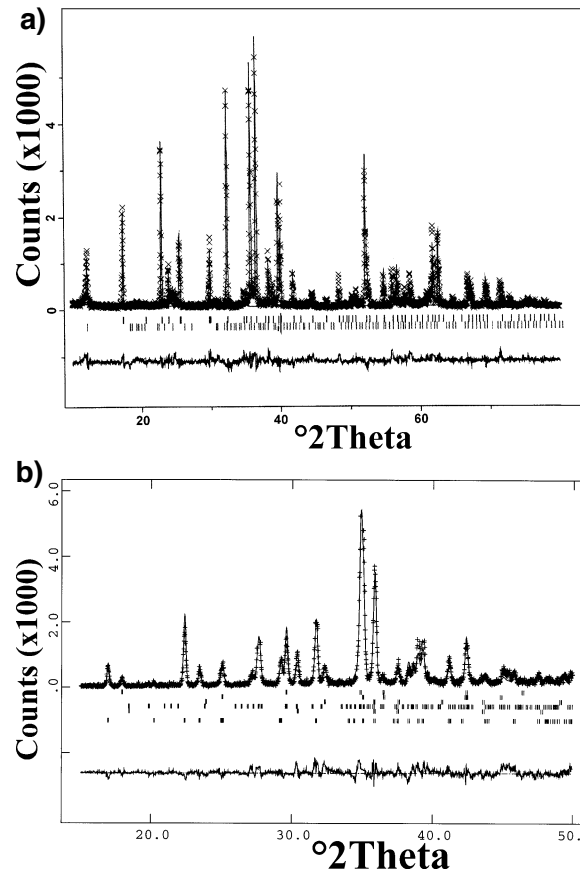

FIGURE 1. A selected region of the observed and calculated patterns, and difference curve, of the investigated olivine sample. (**a**) At room temperature. (lower row of markers = serpentine, upper row of markers = olivine. (**b**) At 1270 °C. (from the bottom upward, the markers are: first row = olivine, second row = magnetite, third row = proto-enstatite, fourth row = hematite, fifth row = alumina substrate, and sixth row = spinel)

TABLE 2. Results of the quantitative phase analysis with the Rietveld method of the olivine sample at room temperature (RT) and at 1270 °C in situ

Phase	Olivine R *T* (wt%)	Olivine 1270 °C (wt%)
Olivine	97.8(5)	62.8(7)
Serpentine (Lizardite)	2.2(5)	–
Proto-enstatite	–	22.7(8)
Ematite	–	4.7(8)
magnetite	–	9.0(7)
Ferrochromite-hercynite	–	0.8(4)

JMA equation to the non-isothermal data for the decomposition of hematite and growth of pyroxene. Figures 4a and 4b illustrate α-time plots for the formation of hematite during the isothermal run at 800 °C and a relative logarithmic plot using the Avrami equation for the calculation of the reaction order coefficient n [1.83(5) with $r^2 = 0.95$]. Figure 4c illustrates y(α) and z(α) vs. α plots showing that the non-isothermal and the isothermal runs match perfectly, thus validating the application of the JMA model for the non-isothermal run (Malek and Mitsuhashi 2000). In fact, the extension of the validity of the JMA model from isothermal to non-isothermal conditions implies that the plots of the non-isothermal and the isothermal runs are coincident [Fig. 4c, according to the Malek and Mitsuhashi (2000) formalism].

The result of the best-fit analysis using the methods of CR and KC shows that the most likely rate-limiting step for the formation of hematite is diffusion, although the methods are not sensitive enough to discriminate among the various diffu-

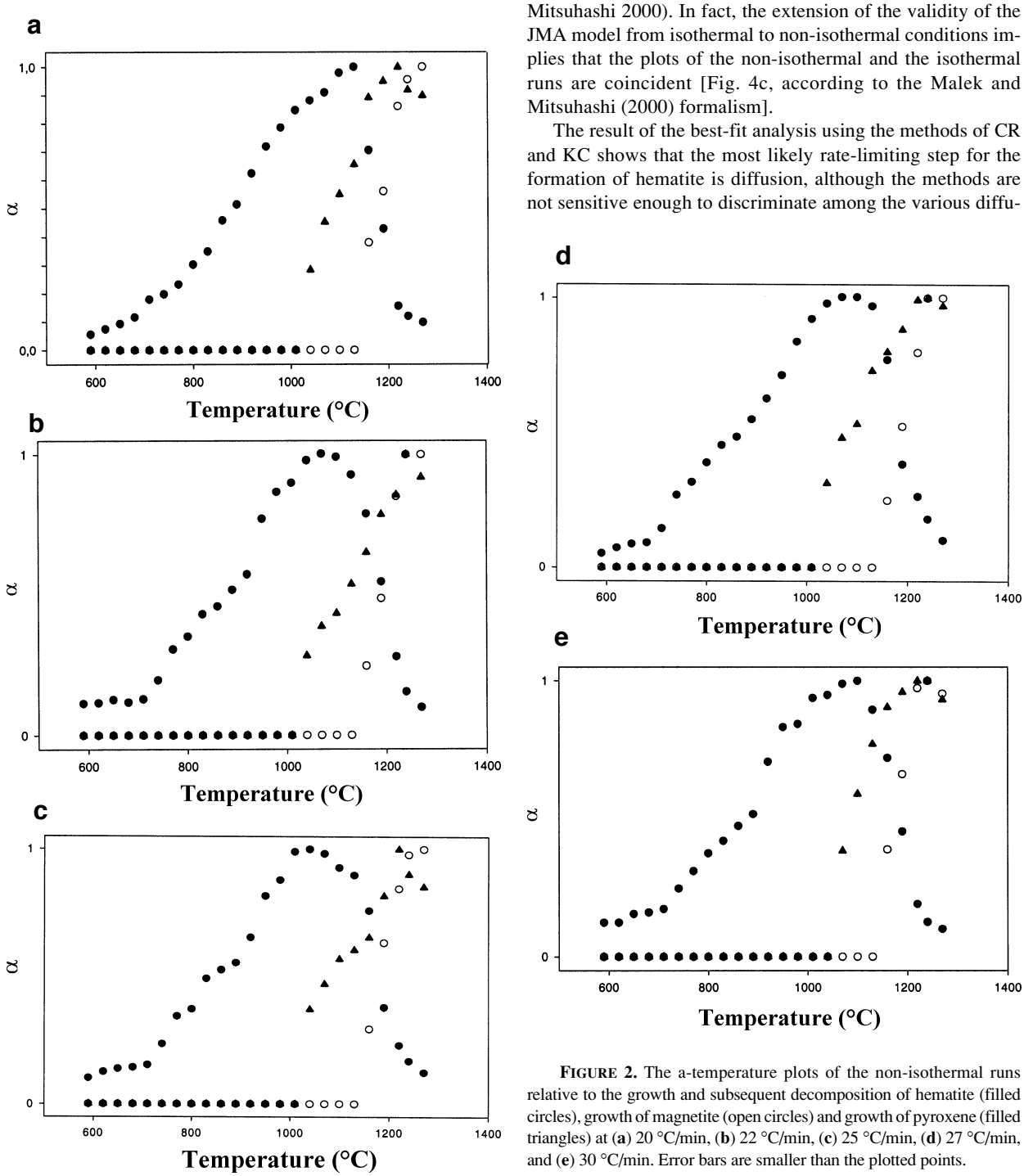

FIGURE 2. The a-temperature plots of the non-isothermal runs relative to the growth and subsequent decomposition of hematite (filled circles), growth of magnetite (open circles) and growth of pyroxene (filled triangles) at (**a**) 20 °C/min, (**b**) 22 °C/min, (**c**) 25 °C/min, (**d**) 27 °C/min, and (**e**) 30 °C/min. Error bars are smaller than the plotted points.

sion mechanisms (D1, D2, D3, or D4). The Avrami plot for the isothermal data suggests two-dimensional diffusion and a constant or decelerating nucleation rate with $n \approx 1.8$. The fit of the α-time plot using the Avrami equation with $n = 1.8$ [$\alpha = 1 - \exp(-kt)^{1.8}$] yielded $k = 0.008(2)$ The apparent activation energy calculated using the Kissinger method is 15 kcal/mol.

The rate-limiting step for the formation of pyroxene is also diffusion. The result of the best-fit analysis using the methods of CR and KC seems insensitive, although generally indicating a diffusion-limited mechanism (D1–D4). In some cases, other mechanisms may be possible (e.g., R2–R3 at 20 °C or A2–A4 at 30 °C), but the JMA model again points to two-dimensional diffusion with decelerating nucleation rate with $n \approx 1.72$ and a calculated apparent activation energy of 29 kcal/mol.

The kinetic reaction of hematite decomposition and magnetite formation coincides. According to the JMA model, the hematite to magnetite transformation is governed by a contracting volume, interface-controlled reaction in two or three dimensions. The apparent activation energy calculated independently with the Kissinger method is 30 kcal/mol for magnetite growth and 31 kcal/mol for hematite decomposition. Once again, the results of the analysis using the methods of CR and KC seem insensitive. In fact, although these methods generally indicate a contracting volume mechanism (R2–R3), in some runs, alternative mechanisms seem equally possible (e.g., A2–A4).

TABLE 3. Result of the best fit analysis using the methods of Coats and Redfern (CR) and Kennedy and Clark (KC) using the kinetic functions reported in Table 1

Reaction (method)	20 °C/min Equation, R^2, χ^2, F-test	22 °C/min Equation, R^2, χ^2, F-test	25 °C/min Equation, R^2, χ^2, F-test	27 °C/min Equation, R^2, χ^2, F-test	30 °C/min Equation R^2, χ^2, F-test
Hematite growth (CR)	A2, 0.987, 0.15, 2.515 R2, 0.993, 0.11, 2.826 R3, 0.992, 0.12, 2.759 D2, 0.992, 0.12, 2.759 D3, 0.994, 0.11, 2.903 D4, 0.994, 0.11, 2.903 F1, 0.987, 0.15, 2.515	D1, 0.951, 0.45, 1.842 D2, 0.982, 0.18, 2.351 D3, 0.966, 0.30, 2.029 D4, 0.977, 0.22, 2.227	D1,0.965, 0.33, 2.014 D2, 0.961, 0.38, 1.959 D4, 0.964, 0.34, 1.999	R2, 0.971, 0.28, 2.109 R3, 0.974, 0.27, 2.165 D1, 0.952, 0.43, 1.853 D2, 0.974, 0.22, 2.165 D3, 0.980, 0.19, 2.298 D4, 0.977, 0.20, 2.227 F1,0.968, 0.24, 2.059	R2, 0.956, 0.39, 1.897 D1, 0.967, 0.24, 2.044 D2, 0.968, 0.24, 2.059 D3, 0.959, 0.35, 1.933 D4, 0.970, 0.25, 2.092
Hematite growth (KC)	D1, 0.973, 0.25, 2.146 D2, 0.985, 0.16, 2.443 D3, 0.980, 0.17, 2.298 D4, 0.988, 0.14, 2.555	D1, 0.953, 0.41, 1.863 D2, 0.972, 0.23, 2.127 D4, 0.961, 0.33, 1.959	D1, 0.955, 0.42, 1.886 D2, 0.965, 0.29, 2.014	D2, 0.956, 0.40, 1.897 D3, 0.962, 0.38, 1.972 D4, 0.960, 0.39, 1.946	D1, 0.960, 0.39, 1.946 D2, 0.962, 0.40, 1.972 D3, 0.959, 0.41, 1.933 D4, 0.951, 0.45, 1.842
Hematite decomposition (CR)	R2, 0.974, 0.05, 2.165 R3, 0.969, 0.06, 2.076 D1, 0.964, 0.05,1.999 D2, 0.951, 0.08, 1.842 D3, 0.967, 0.05, 2.044 D4, 0.973, 0.05, 2.146	A2, 0.988, 0.03, 2.555 R2, 0.954, 0.07, 1.874 R3, 0.967, 0.05, 2.044 D2, 0.966, 0.05, 2.029 D3, 0.965, 0.05, 2.014 F1, 0.988, 0.03, 2.555	A2, 0.965, 0.05, 2.014 D1, 0.954, 0.07, 1.874 D2, 0.956, 0.07, 1.897 F1, 0.965, 0.05, 2.014	A2, 0.988, 0.03, 2.555 R2, 0.990, 0.03, 2.647 R3, 0.990, 0.03, 2.647 D2, 0.990, 0.03, 2.647 D3, 0.993, 0.02, 2.826 D4, 0.992, 0.02, 2.759	R2, 0.973, 0.05, 2.146 R3, 0.984, 0.04, 2.410 D2, 0.970, 0.06, 2.092 D3, 0.983, 0.04, 2.379 D4, 0.964, 0.05, 1.999 F1, 0.980, 0.04, 2.297
Hematite decomposition (KC)	A2, 0.955, 0.07, 1.886 R2, 0.960, 0.06, 1.946 R3, 0.958, 0.06, 1.921 D1, 0.960, 0.06, 1.946 D2, 0.957, 0.07, 1.909	A2, 0.997, 0.01, 3.250 R2, 0.994, 0.02, 2.903 R3, 0.996, 0.01, 3.106 D1, 0.967, 0.05, 2.044 D2, 0.975, 0.06, 2.185 D3, 0.988, 0.03, 2.555 D4, 0.979, 0.05, 2.273	A2, 0.991, 0.02, 2.700 R2, 0.991, 0.02, 2.798 R3, ,0.991, 0.02, 2.699 D1, 0.970, 0.06, 2.092 D2, 0.972, 0.05, 2.127 D3, 0.978, 0.05, 2.249 D4, 0.974, 0.06, 2.165	A2, 0.992, 0.02, 2.759 R2, 0.997, 0.01, 3.250 R3, 0.996, 0.02, 3.106 D1, 0.984, 0.04, 2.410 D2, 0.988, 0.03, 2.555 D3, 0.991, 0.02, 2.699 D4, 0.989, 0.03, 2.599	A2, 0.985, 0.04, 2.443 R2, 0.988, 0.03, 2.555 R3, 0.987, 0.03, 2.515 D1, 0.984, 0.04, 2.410 D2, 0.985, 0.04, 2.443 D3, 0.985, 0.04, 2.443 D4, 0.985, 0.04, 2.443
Magnetite growth (CR)	A2, 0.988, 0.03, 2.555 R2, 0.972, 0.07, 2.127 R3, 0.993, 0.02, 2.826 D2, 0.989, 0.03, 2.599 D3, 0.993, 0.02, 2.826 D4, 0.960, 0.06, 1.946 F1, 0.988, 0.03, 2.555	A2, 0.995, 0.02, 2.994 D2, 0.998, 0.01, 3.453 D3, 0.997, 0.01, 3.250 F1, 0.995, 0.02, 2.994	A2, 0.988, 0.03, 2.555 R3, 0.968, 0.05, 2.059 D2, 0.953, 0.08, 1.863 D3, 0.970, 0.06, 2.092 F1, 0.988, 0.03, 2.555	A2, 0.997, 0.03, 3.250 D2, 0.986, 0.04, 2.477 F1, 0.997, 0.01, 3.250 F2, 0.961, 0.06, 1.959 F3, 0.963, 0.06, 1.986	A2, 0.981, 0.04, 2.323 R2, 0.983, 0.05, 2.379 R3, 0.996, 0.02, 3.106 D2, 0.996, 0.02, 3.106 D3, 0.996, 0.02, 3.106 F1, 0.981, 0.04, 2.323
Magnetite growth (KC)	R3, 0.963, 0.07, 1.986 D2, 0.978, 0.05, 2.249 D3, 0.989, 0.03, 2.599	A2, 0.991, 0.03, 2.700 D2, 0.997, 0.01, 3.250 D3, 0.992, ‘0.03, 2.759	R3, 0.959, 0.06, 1.933 D2, 0.977, 0.05, 2.227 D3, 0.968, 0.05, 2.059	A2, 0.962, 0.02, 1.972 R3, 0.973, 0.07, 2.146 D2, 0.986, 0.04, 2.477 D3, 0.980, 0.04, 2.298	R3, 0.980, 0.04, 2.297 D2, 0.994, 0.02, 2.903 D3, 0.993, 0.02, 2.826 D4, 0.966, 0.07, 2.028
Pyroxene growth (CR)	A2, 0.974, 0.05, 2.165 R2, 0.980, 0.04, 2.298 R3, 0.983, 0.03, 2.380 D2, 0.991, 0.02, 2.700 D3, 0.985, 0.03, 2.443 D4, 0.976, 0.05, 2.205 F1, 0.974, 0.05, 2.165	A2, 0.986, 0.02, 2.477 R2, 0.959, 0.07, 1.933 D1, 0.990, 0.02, 2.647 D2, 0.990, 0.02, 2.647 D4, 0.978, 0.04, 2.249 F1, 0.986, 0.03, 2.477	D1, 0.960, 0.07, 1.946 D2, 0.952, 0.09, 1.853	R2, 0.977, 0.04, 2.227 R3, 0.978, 0.04, 2.249 D2, 0.963, 0.06, 1.986 D2, 0.981, 0.04, 2.323 D4, 0.975, 0.05, 2.185	A2, 0.990, 0.02, 2.647 R3, 0.972, 0.05, 2.127 D3, 0.976, 0.05, 2.205 F1, 0.990, 0.02, 2.647 F2, 0.967, 0.06, 2.044 F3, 0.969, 0.06, 2.075
Pyroxene growth (KC)	D2, 0.951, 0.09, 1.842 D3, 0.964, 0.06, 1.999 D4, 0.966, 0.06, 2.039	D2, 0.956, 0.08, 1.897 D3, 0.957, 0.08, 1.909 D4, 0.957, 0.08, 1.909	D1, 0.989, 0.02, 2.599 D2, 0.993, 0.01, 2.826 D3, 0.989, 0.02, 2.599 D4, 0.992, 0.01, 2.759	D3, 0.951, 0.09, 1.842 D4, 0.951, 0.09, 1.842	D3, 0.972, 0.05, 2.127 D4, 0.954, 0.08, 1.874

Note: Only the results of the fitting procedure with $r^2 > 0.95$ are reported. ν are the degrees of freedom.

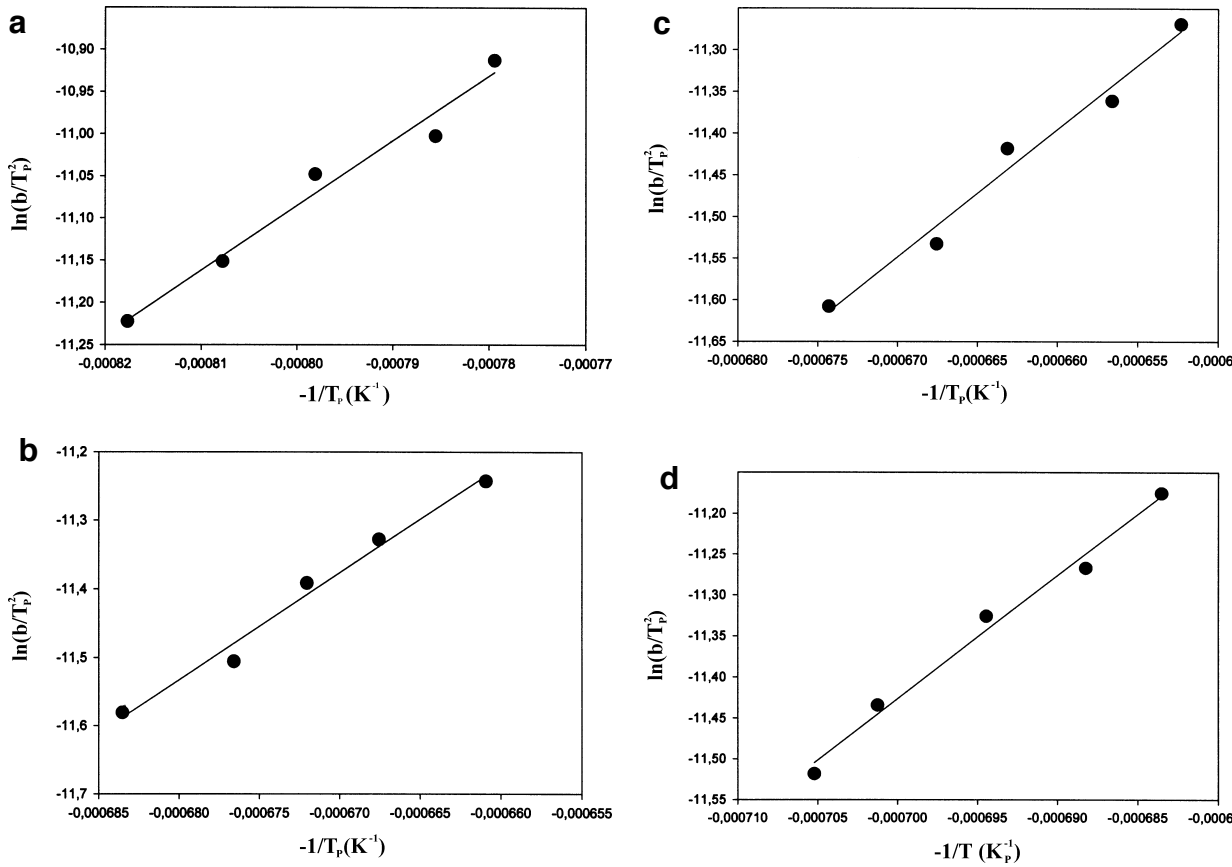

FIGURE 3. The logarithmic plot calculated using the Kissinger method (Bamford and Tipper 1980) relative to the growth (**a**) and subsequent decomposition of hematite (**b**), growth of magnetite (**c**), and growth of pyroxene (**d**). Error bars are smaller than the plotted points.

TABLE 4. Apparent activation energies (E_a) and relative regression coefficients calculated with the Kissinger method (see text for details)

	hematite growth	hematite decomposition	magnetite growth	pyroxene growth
E_a (kcal/mol)	15(3)	31(5)	30(3)	29(3)
R^2	0.974	0.983	0.979	0.988
χ^2	0.049	0.029	0.032	0.025

TABLE 5. Calculation of the Avrami coefficient n and relative regression coefficients using the JMA model for the decomposition of hematite and growth of pyroxene (see text for details)

b (°C/min)	hematite R^2	decomposition m	pyroxene R^2	growth m
20	0.894	2.52(33)	0.954	1.95(12)
22	0.963	3.40(11)	0.991	1.32(3)
25	0.962	3.30(12)	0.999	1.51(2)
27	0.889	2.60(36)	0.960	1.72(10)
30	0.940	3.10(17)	0.987	2.12(5)
average		2.98		1.72

The TG analysis (Fig. 5) indicates minor weight losses due to the dehydration (about 200 °C) and dehydroxylation (about 600–700 °C) of serpentine and a weight increase above 600 °C due to the oxidation reaction. The DTA analysis shows a broad endothermic peak at temperatures below 600 °C due to the decomposition of serpentine, an exothermic peak due to the oxidation reaction, and an endothermic peak at about 1050 °C due to the nucleation of pyroxene.

The SEM analyses are in agreement with the diffraction data. Figure 6 illustrates selected back-scattered electron (BSE) images of the olivine crystals. Images of the original olivine crystals(Fig. 6a) show a few crystals (white spots) of spinel and veins (dark gray) reflecting alteration to serpentine. The spot EDS analysis indicated that the spinel is a member of the ferrochromite-hercynite series. BSE images of the olivine crystals quenched at 900 °C (Fig. 6b) show that the veins acted as nucleation centers for the growth of hematite. Hematite has a preference to crystallize on defects and fractures (Fig. 6b). At 1100 °C, the quenched crystals show more-extensive crystallization of hematite(Fig. 6c) accompanied by the growth of pyroxene at the olivine grain boundary (Fig. 6d). At 1200 °C, the quenched hematite crystals are partly replaced by magnetite, which grows along preferred directions (black arrow) or in random aggregates (white arrow) (Fig. 6e).

The newly formed phases and their structural relationships with olivine were investigated with TEM on quenched crystals. Two different kinds of precipitates (globular and elongated) can be detected inside olivine in samples treated at 700, 800, and 900 °C (Figs. 7a and 7b). Both are formed by the aggregation of smaller rounded grains that appear darker than olivine matrix in bright-field images. The elongated precipitates nucleate around planar defects usually parallel to the (100) planes. EDS analyses reveals that the precipitates are richer in Fe than

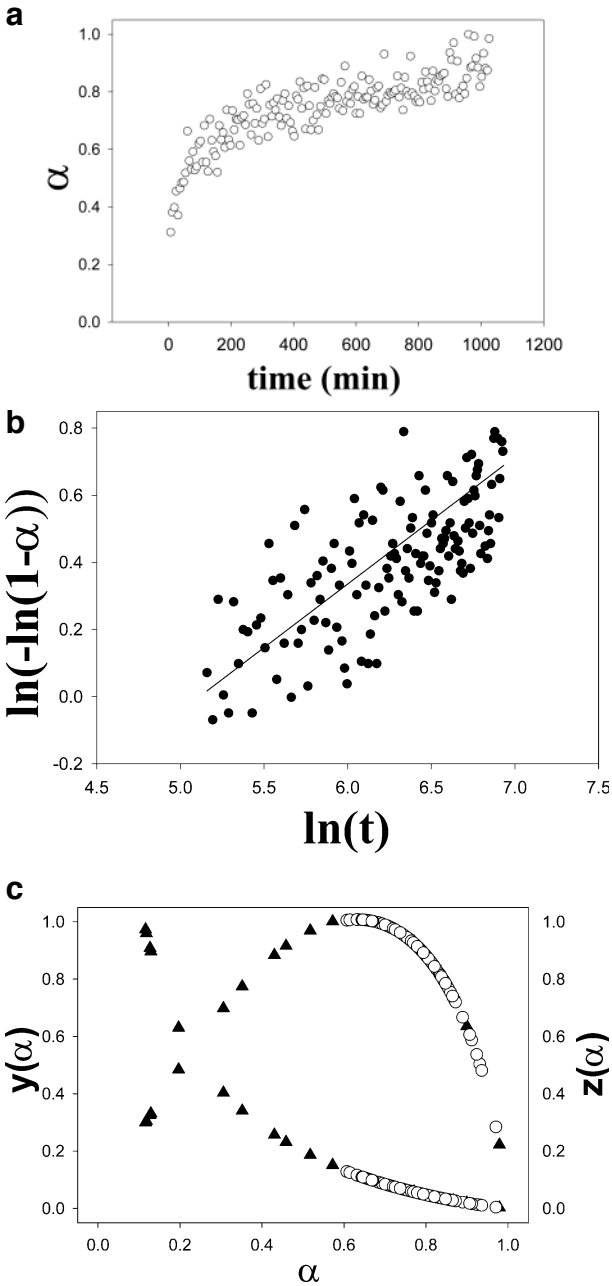

FIGURE 4. The α-time plot for the formation of hematite during the isothermal run at 800 °C, (**a**) and the relative logarithmic plot using the Avrami equation (**b**) for the calculation of the reaction order coefficient *n*. The y(α) and z(α) vs. α plots (**c**) show that the non-isothermal (filled triangles) and the isothermal (open circles) runs match perfectly, demonstrating that the JMA model can be applied (Malek and Mitsuhashi 2000). Error bars are smaller than the plotted points.

the olivine. Because of their small grain size (<200 Å), the precipitates cannot be studied by electron diffraction. Instead, high-resolution electron microscopy (HREM) was used to reveal their structure, and showed that the precipitates are crystalline and usually surrounded by amorphous material. As the precipitates are coherent with olivine, it is possible to obtain

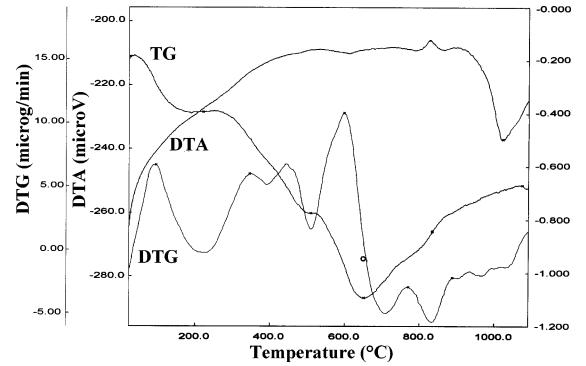

FIGURE 5. The TG, DTG, and DTA analyses of the investigated olivine sample.

very well-resolved, phase-contrast images by orienting the host olivine along a zone axis. By measuring the periodicity observed in these images, the precipitates can be identified as hematite. Their shape is very similar to those observed by Champness (1970), to the "mushroom" hematite-amorphous silica clusters found by Kondoh et al. (1985), and to the (100) precipitate complexes of hematite and laihunite observed by Iishi et al. (1997). In the present case, the topotactic relationship [$(100)_{HE}$ // $(001)_{OL}$ and $(001)_{HE}$ // $(100)_{OL}$] was confirmed and corresponds to the sharing of the framework of hexagonal close-packed O atoms, in agreement with the literature data (Champness 1970).

Figure 8 shows an HREM image of olivine oriented along [210], close to an area of elongated hematite aggregations. A hematite grain is well-resolved, and a comparison with the image simulation confirms its nature. The agreement between the simulation and the image of the olivine displayed in Figure 8 can be improved if a model of ferrifayalite with occupancy of 0.8 for the Fe^{2+} site is considered. This result is an indication that ferrifayalite layers surround the hematite regions (Kondoh et al. 1985), although additional proof is needed since this was the only evidence found. The amorphous material grown around the hematite grains was identified as amorphous silica because in all EDS analyses performed in precipitate regions Si has always been detected, even when the spot was reduced to a minimum size.

Figure 9 shows a HREM image of olivine oriented along [010] near a globular-shaped precipitate. Several grains of hematite are embedded within the olivine matrix. The superposition of the two structures results in a very complicated Fourier transform and image contrast. The stacking of hematite and olivine produces Moiré contrast fringes of nearly 11 Å. These fringes are parallel to both $(101)_{OL}$ and $(10\bar{1})_{OL}$ planes (four small spots around the central beam in the Fourier transform), because several hematite grains are related by a twinning transformation on the $(001)_{HE}$ plane. In fact, in the Fourier transform (inset on the left), reflections corresponding to two different sets of hematite crystals oriented along the $[100]_{HE}$ zone axis can be identified (gray and black circles, respectively). The hematite crystals have the $(200)_{OL}$ and $(002)_{OL}$ reflections in common with the olivine lattice, as expected by the topotactic relationship, and they are related by a mirror plane around $(001)_{HE}$. The remaining reflections that cannot be indexed with

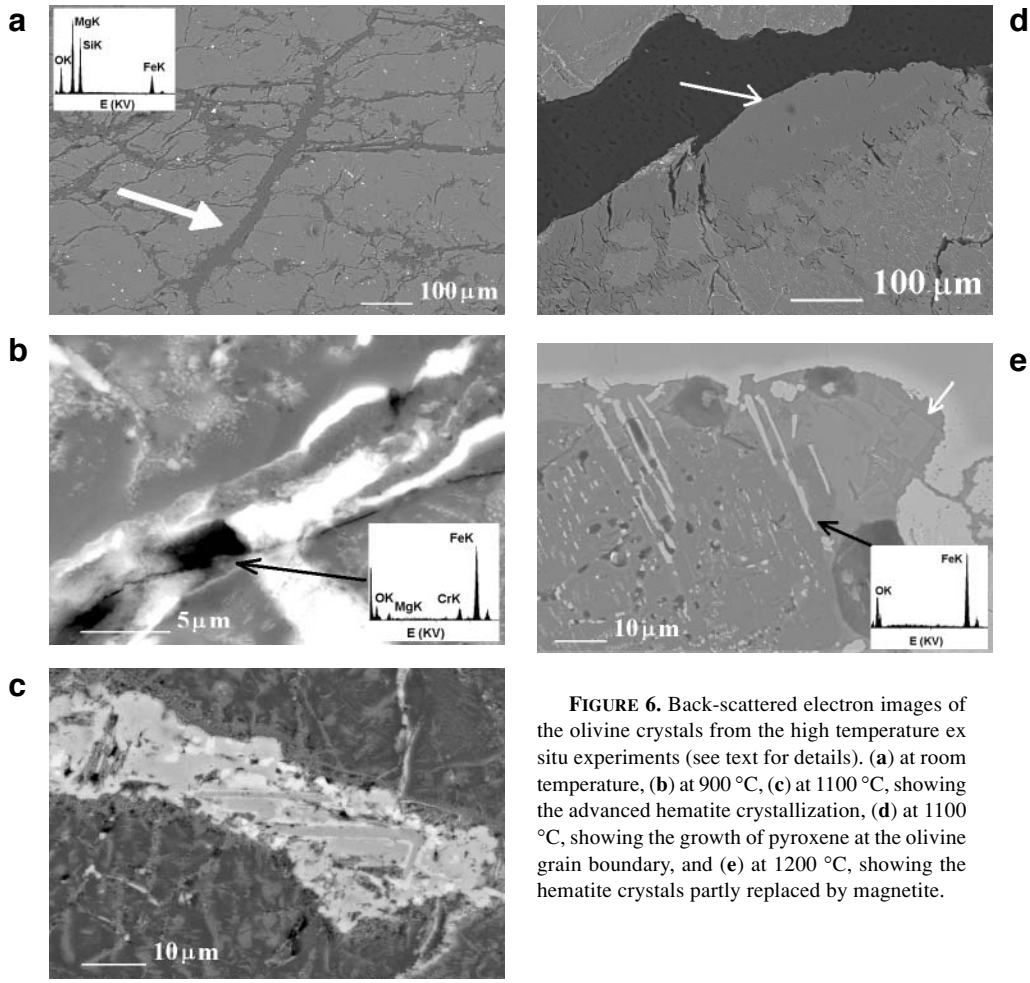

FIGURE 6. Back-scattered electron images of the olivine crystals from the high temperature ex situ experiments (see text for details). (**a**) at room temperature, (**b**) at 900 °C, (**c**) at 1100 °C, showing the advanced hematite crystallization, (**d**) at 1100 °C, showing the growth of pyroxene at the olivine grain boundary, and (**e**) at 1200 °C, showing the hematite crystals partly replaced by magnetite.

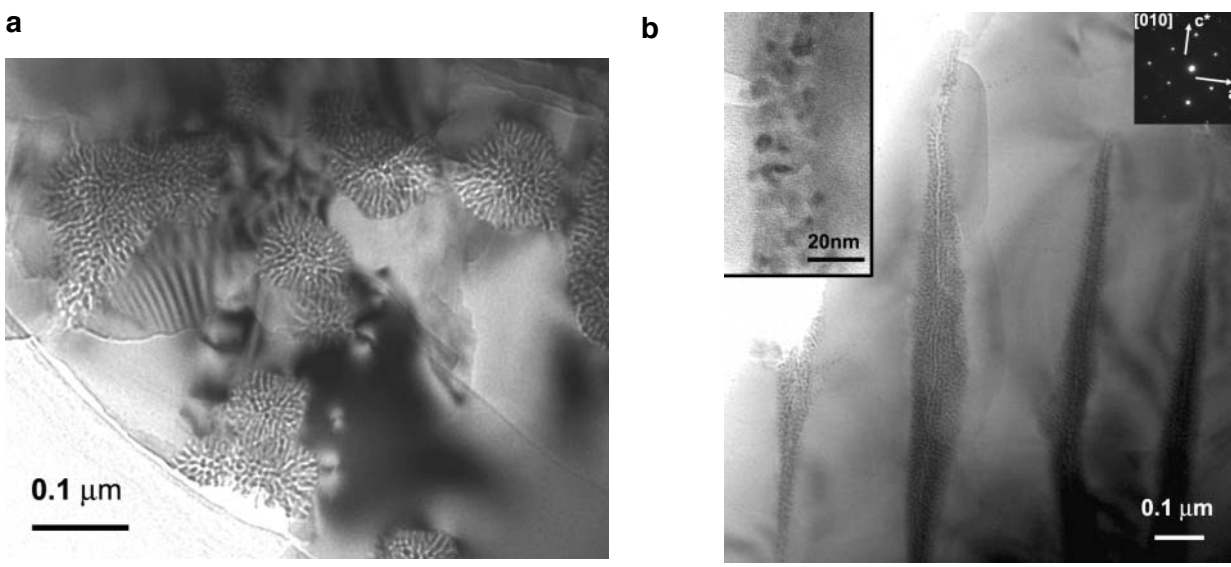

FIGURE 7. (**a**) Bright-field image of globular-shaped hematite precipitates in olivine treated at 800 °C. (**b**) Bright-field image of elongated hematite precipitates in olivine treated at 800 °C. The image is taken along [010]. The precipitates have grown parallel to the [001] direction, as can be seen by the SAED pattern shown in the inset (top right). The other inset on the left shows a magnified image of a precipitate in a sample treated at 700 °C. Individual crystals are clearly visible, and their grain size is around 10 nm.

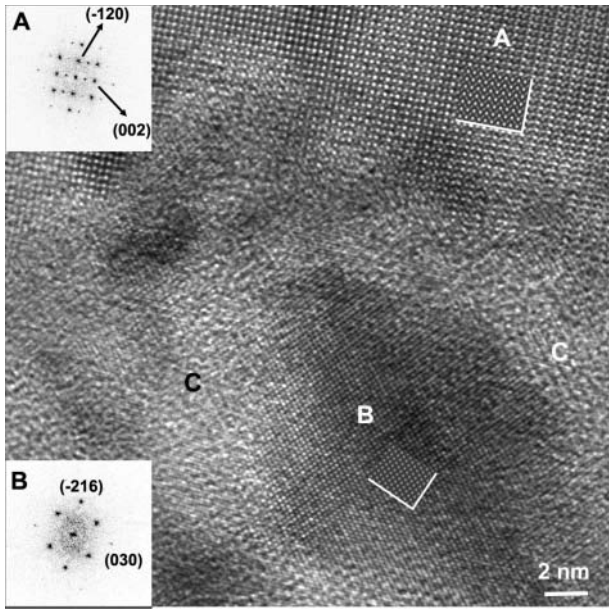

FIGURE 8. HREM image taken on the boundary between olivine and a precipitate region on a sample treated at 900 °C. The olivine is oriented along zone axis [210]. The olivine (region A) is shown in the upper part of the image. The Fourier transform calculated in this area is displayed in the inset at the top left. An image simulation of olivine calculated for a thickness of 230 Å is added for comparison. In the lower part, a crystal grain of hematite (region B) embedded in amorphous material (region C) can be seen. The Fourier transform calculated in this area (inset B bottom left) shows that the hematite is oriented along [301]. A good match with an image simulation (inset superimposed on the hematite crystal) is obtained for a thickness of 60 Å. Both the simulations have been calculated with the same defocus of 55 nm.

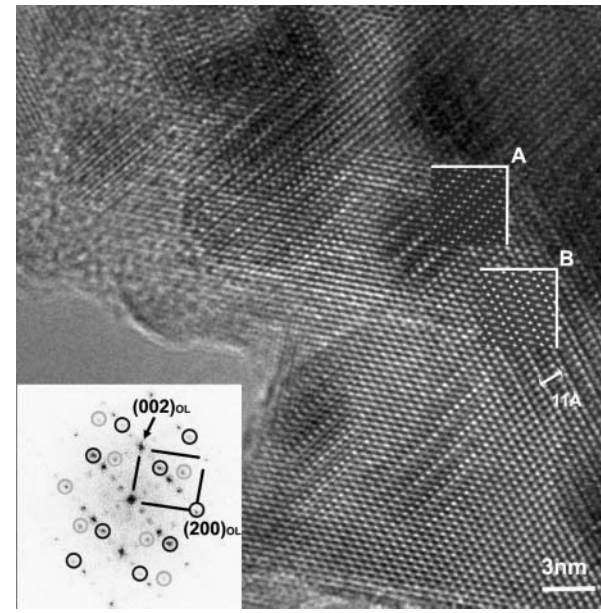

FIGURE 9. HREM image of olivine treated at 800 °C taken on a globular precipitate. Several hematite grains embedded in olivine can be identified as darker rounded areas where the contrast exhibits fringes with longer periodicity (~11 Å). In the Fourier transform of the image (inset bottom left), the centered reciprocal lattice plane [010] of olivine is drawn with segments. The circled spots are due to two different sets of hematite grains oriented in $[100]_{HE}$ and connected by a twinning transformation on $(001)_{HE}$. In fact, the reflection $(200)_{OL} = (006)_{HE}$ belongs to both twinned lattices. Regions A and B are image simulations of the stacking of olivine and hematite obtained following the model described in the text.

the olivine or hematite reciprocal lattices are due to double-diffraction and create the Moiré fringes. To confirm this interpretation, image simulations were performed. The program EMS accepts stacking sequences of commensurate super-cells of different crystal structures. Therefore, a common orthorhombic super cell with $\mathbf{a} = 3\mathbf{a}_{OL} = \mathbf{c}_{HE} \sim 14.4$ Å, $\mathbf{b} = \mathbf{b}_{OL} = 2\mathbf{b}_{HE} \sim 10$ Å, and $\mathbf{c} = 3\mathbf{c}_{OL} = 2\sqrt{3}\mathbf{a}_{HE} = 17.5$ Å, was converted into $P1$ symmetry for both olivine and hematite. Subsequently different stacking sequences were tried along **b** of olivine and hematite super-cells to reproduce the image contrast. The simulation displayed in inset A was obtained by stacking 30 super-cells of olivine and 5 of hematite for a total thickness of 350 Å. The simulation shown in inset B was obtained by stacking 15 super-cells of olivine, 5 super-cells of hematite, and 15 super-cells of olivine for the same total thickness. In this case, the hematite structure has been mirrored with respect to $(001)_{HE}$, because the contrast fringes are parallel to $(101)_{OL}$ and not to $(\bar{1}01)_{OL}$ as in the previous case. Both simulations have the same defocus of 115 nm. As can be seen, the agreement is quite good in both cases and confirms the interpretation.

Pyroxene crystals were observed with TEM in the samples treated at 1200 °C (Fig. 10). Pyroxene grains have size of 0.3–0.5 mm and are always quite disordered. Selected area diffraction patterns taken in the [010] direction show streaking parallel to $(h00)$ (see the inset of Fig. 10). The spots connected by the streaks can be indexed using both a protoenstatite or a clinoenstatite unit cell. Reflections that require doubling of the **a** axis (orthoenstatite) to be indexed were not detected. On an atomic scale, pyroxene appears as a disordered stacking of the characteristic 4.5 Å modules along (100) (Putnis and McConnell 1980), as can be seen in Figure 10. In a few cases, small ordered domains of clinoenstatite have been found, which have a very small size (<500 Å) and are coherent with disordered areas. No topotactic relationship has been observed between the pyroxene crystals and the surrounding olivine. This finding is not completely in disagreement with that claimed by Champness (1970), who observed two different possible orientations of pyroxene in olivine ($(100)_{OL} \parallel (100)_{PX}$, $\mathbf{b}_{OL} \parallel \mathbf{c}_{PX}$, $\mathbf{c}_{OL} \parallel \mathbf{b}_{PX}$ and $(100)_{OL} \parallel (100)_{PX}$, $\mathbf{b}_{OL} \parallel \pm [011]_{PX}$, $\mathbf{c}_{OL} \parallel \pm [01\bar{3}]_{PX}$), although he also reported that the "… preferred orientation of the pyroxene with respect to the parent olivine is poor (p. 799)."

Samples treated at 1300 °C shows the presence of magnetite grains dispersed in the olivine matrix. TEM observations were quite difficult due to the absence of clear precipitate structures. The magnetite grains always show the topotactic relation $(100)_{OL}$ // $(111)_{MT}$ and $(001)_{OL}$ // $(110)_{MT}$ with olivine. A selected area diffraction taken on one of these grains is displayed in Figure 11. Spots belonging to $[010]_{OL}$ olivine and

$[211]_{MT}$ magnetite reciprocal lattice planes can be detected on the same plate. In this projection, the two reciprocal lattices are geometrically coincident but the aspect of $[010]_{OL}$ is completely different from what we observe. The ($h0l$) reflections with $h + l = 2n + 1$ should be extinct as they cannot be switched on by dynamical effects, whereas in Figure 11b, several of these forbidden reflections are clearly visible. This result can be explained only by the superposition of $[010]_{OL}$ and $[211]_{MT}$ patterns as can be seen by comparison with the inset on the left. The crystal is elongated along the $[011]_{MT}$ direction and seems to have grown from a $(100)_{OL}$ plane (see again Fig. 11).

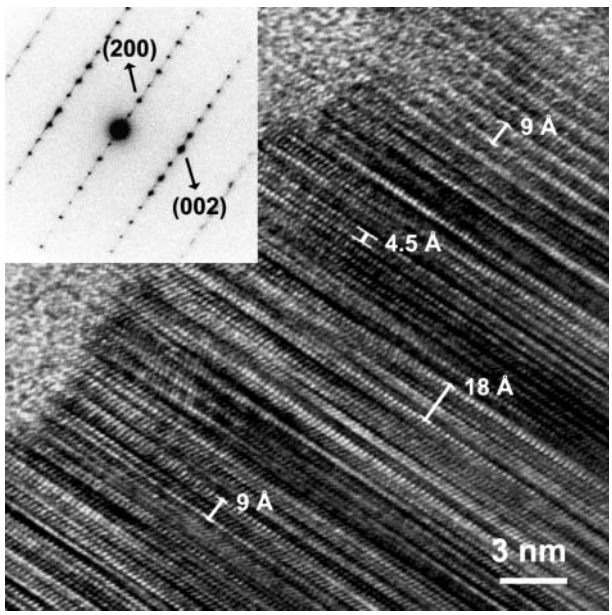

FIGURE 10. HREM image of an enstatite crystal oriented along [010]. The structure is a disordered stacking normal to (100) of modules 4.5 Å thick: the basic building blocks of pyroxenes (one of these is marked in the center of the image). In different regions of the image, ordered subunits of 9 Å and 18 Å can be identified (they are indicated by markers for clarity). The inset shows an SAED pattern taken on the same region. It is indexed as clinoenstatite, and exhibits rather strong streaks along (h00) indicating that the disorder extends over a large area.

DISCUSSION

At about 600 °C, hematite is the first newly formed phase in the reaction sequence:

$$(Mg_{0.84}Fe^{2+}_{0.16})_2SiO_4 + 0.08O_2 \rightarrow 0.16Fe^{3+}_2O_3 + 0.84Mg_2SiO_4 + 0.16SiO_2$$

One of the reaction products is amorphous silica, which recombines later with forsterite to form pyroxene. Hematite is stable up to 1130 °C, the temperature at which magnetite starts to crystallize. Thus, above 1130 °C, two independent transformations are observed, the formation of pyroxene, which is stable up to 1240 °C, and the formation of magnetite according to the reactions:

$$0.16Mg_2SiO_4 + 0.16SiO_2 \rightarrow 0.16Mg_2Si_2O_6$$
$$1.333Fe^{3+}_2O_3 \rightarrow Fe^{2+}Fe^{3+}_2O_4$$

The sequence is in agreement with those reported in the temperature range 700–1100 °C by Koltermann (1962), Champness (1970), Wu and Kohlstedt (1988), and Khisina et al. (2000). At lower temperature (600–700 °C), the TEM study of Khisina et al. (1995, 1998) revealed the presence of laihunite inside the reacting grains of olivine and magnesioferrite at their surface, for which they postulate the following reaction sequence: olivine → laihunite + magnesioferrite → hematite, with the planar defects of laihunite within the olivine matrix acting as preferred pathways for the diffusion of O atoms and, consequently, for the oxidation reaction. Here, SEM and TEM did not show any evidence for the presence of laihunite as a precursor of hematite. This result is not surprising because, according to Khisina et al. (1999), laihunite appears as planar defects inside olivine matrix under oxidation in air at 700–750 °C, which obviously cannot be seen by PXRD.

The rate-limiting step for the formation of hematite is a two-dimensional diffusion with a constant or decelerating nucleation rate and apparent activation energy of 15 kcal/mol. This scenario is compatible with a reaction model whose rate limiting step is anisotropic diffusion of the Fe and/or Mg species. Anisotropic diffusion in minerals was already reported by Ingrin et al. (2001), who measured the anisotropic diffusion of O in

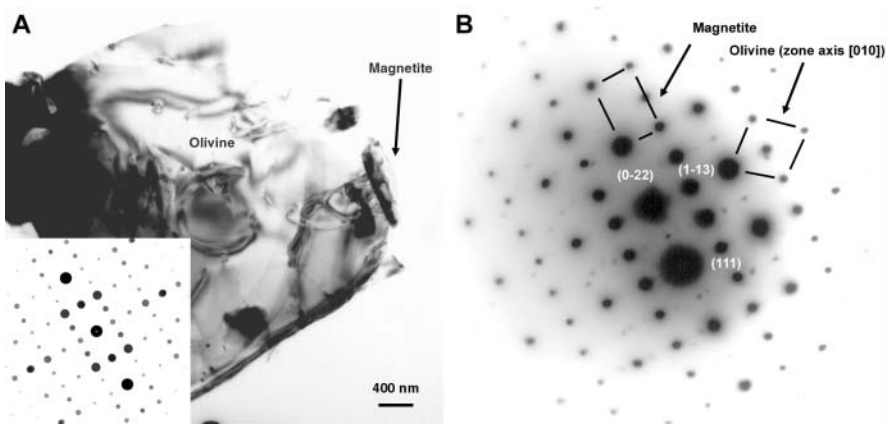

FIGURE 11. (**a**) Bright-field image of a fragment of olivine treated at 1300 °C. A magnetite grain is visible at the right as indicated by the arrow. (b) SAED pattern of the previous olivine fragment with the diaphragm selecting an area including the magnetite grain. Spots belonging to both $[010]_{OL}$ and $[211]_{MT}$ zone axes are present in the diffraction pattern. In the inset on the left, a calculated SAED pattern, representing a kinematic approximation of superposed $[010]_{OL}$ and $[211]_{MT}$, is shown for comparison.

diopside. In our olivine sample, diffusion takes place along the **a** and **c** directions and not along **b** where it is hindered by the Si-centered tetrahedra found along that path. This is in agreement with earlier observation on temperature-dependent diffusion of Fe in fayalite: Aggarwal et al. (1997) in particular showed that the highest electrical conductivity in fayalite single crystals is observed along the 001 direction, followed by the 100 direction, and the lowest along the 010 direction (see Fig. 4 on page 324 in Aggarwal et al. 1997). In concert, Mackwell (1992) reports a rate of oxidation of fayalite in air at 770 °C limited by the diffusion of Fe from the internal reaction front to the gas-solid interface through the iron oxide.

The calculated value of the activation energy points toward diffusion of Fe^{3+} species in a highly defective matrix and not to diffusion of Fe^{2+} or Mg^{2+} in the olivine lattice. In fact, 15 kcal/mol is close to the value (about 18 kcal/mol) calculated by Galwey (1997) for the diffusion of Fe^{3+} in the highly defective structure $Fe^{3+}(\square_{1/3}Fe^{3+}_{5/3})S_4$ with immobile S and O species, and much lower than the values reported for the diffusion of Fe^{2+} and/or Mg^{2+} (about 54 kcal/mol: Chakraborty 1997) in an Fo_{86} olivine lattice. Thus, it is not possible to preclude the possibility that the metastable, highly defective phase where Fe^{3+} diffusion takes place, could be at least in part laihunite. Accordingly, Khisina et al. (1998) reported a diffusion-limited reaction and an activation enthalpy of 17(1) kcal/mol for the formation of laihunite from fine-grained Fa_{11} olivine in air at 600 °C, which is nearly identical to the value reported here. Hence, this issue remains open to debate.

The TEM images (Fig. 7a and 7b) exhibit hematite nuclei that correspond with amorphous silica regions, thus corroborating the evidence that the precursor of hematite is an Fe-silicate poor in Mg. The concentration of Fe^{3+} in Fe-rich, Mg-depleted regions leads to the heterogeneous nucleation of hematite, which may be favored by the presence of defects or grain boundaries with impurity phases such as serpentine. In fact, the SEM images (Fig. 6b) clearly show that hematite appears in the serpentine-filled fractures in the olivine crystals. It is well known that serpentine is unstable at those temperatures and may be highly reactive. MacKenzie and Meinhold (1994) and Treiman (1998) showed that the reactions at temperatures higher than 600 °C involving serpentine are dehydroxylation:

$$Mg_3Si_2O_5(OH)_4 \rightarrow Mg_3Si_2O_7 + 2H_2O$$

and the formation of forsterite and pyroxene:

$$Mg_3Si_2O_7 \rightarrow Mg_2SiO_4 + MgSiO_3$$

At 1130 °C, magnetite begins to crystallize at the expense of hematite with a contracting-volume, interface-controlled reaction in two or three dimensions. The apparent activation energy for the growth of magnetite is 30 kcal/mol and for the decomposition of hematite is 31 kcal/mol. The transformation is direct, with no metastable amorphous intermediate compound. This result is clearly explained with the aid of Figure 12, showing the region of the α-time plot in the range 1100–1300 °C during the hematite to magnetite transformation in the ramp at 20 °C/min. The two curves cross exactly at α = 50% ($\alpha\%_{HEM} + \alpha\%_{MAG} = 100$) indicating that hematite fully transforms into magnetite. In fact, the existence of an intermediate phase would results in a crossover of the curves with $\alpha\%_{HEM} + \alpha\%_{MAG} < 100$.

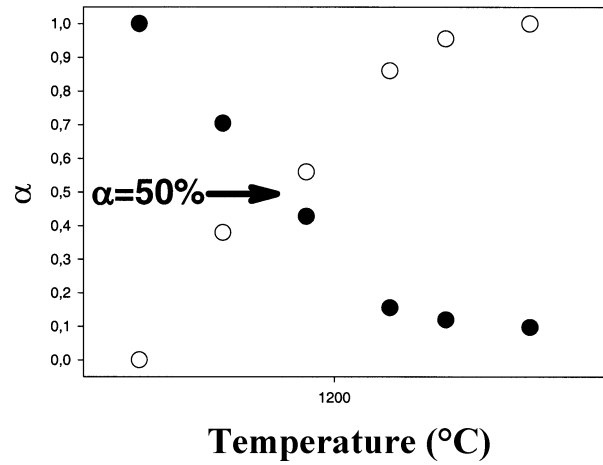

FIGURE 12. The region of the α-time plot in the range 1100–1300 °C during the hematite to magnetite transformation with a heating rate of 20 °C/min. Legend: filled circles = hematite; open circles = magnetite.

The hematite-magnetite transformation is well-described in the literature (Ahra et al. 1995; Janowski et al. 1996; Chakraborthy 1997) by the "shrinking core model," which involves the formation of a magnetite outer layer at the surface of the hematite particles. The reaction proceeds toward the core of hematite by diffusion of the O species throughout the newly formed magnetite layer. The rate of the reaction is limited by advance of the reaction front in two or three dimensions. Magnetite grows along preferred (aligned) directions, in agreement with earlier observations that a spinel-like phase (magnetite) grows as needles (Champness 1970) or in random aggregates (Fig. 6e). Magnetite shows the topotactic relation $(100)_{OL}$ // $(111)_{MT}$ and $(001)_{OL}$// $(110)_{MT}$ with olivine (Fig. 11). The growth mechanism seems totally different with respect to the one proposed for naturally oxidized olivine by Putnis (1979). That author described no orientation relationship between magnetite and olivine but an orientation relationship between the magnetite and the pyroxene regions, which indicates a cooperative nucleation and growth mechanism of the two phases that is not observed here.

Simultaneously, pyroxene is formed from a solid-state reaction between residual forsterite and amorphous silica. The latter was released during the formation of hematite from olivine. The rate-limiting step for the formation of pyroxene is a two-dimensional diffusion with decelerating nucleation rate and apparent activation energy of 29 kcal/mol. A diffusion mechanism was already postulated by Champness (1970) for the formation of enstatite from fayalite and by Fisler et al. (1997) for the formation of enstatite from olivine in contact with quartz at high temperature.

Figure 13 illustrates an HREM image showing the enstatite (En) and olivine (Ol) relationship. The Fourier transform (inset) shows that the olivine is oriented along [112] and the enstatite along [010].

Our TEM observations showed that pyroxene is not formed inside the olivine grains but mainly at grain boundaries. This feature is a very important detail, considering the possible diffusion mechanism. If pyroxene were to nucleate and grow inside the olivine matrix, then the Si and O species should diffuse within the olivine lattice to the growing pyroxene phase. However, this process is not possible because the measured activation energies and enthalpies for the diffusion of Si within the olivine lattice (not lower than 69 kcal/mol: Béjina and Jaoul 1997) are much larger than the activation energy inferred from this kinetic study (29 kcal/mol). This value is, instead, very similar to the activation enthalpy (29.4 kcal/mol) calculated for the diffusion of Si in diopside in the range 1040–1250 °C (Béjina and Jaoul 1997). Hence, pyroxene should have formed at the grain boundary between olivine and amorphous silica and should have grown inward toward the core of forsterite. The rate-limiting step of the reaction is the diffusion of the Si species and not the diffusion of the oxygen atoms, which is much faster. Si diffusion is likely favored by many existing point defects and should take place along the **b-c** planes of the newly formed pyroxene phase toward the front of the reaction (the reaction interface pyroxene-forsterite). Of course, diffusion along **a** in pyroxene is blocked by the presence of the tetrahedral chains.

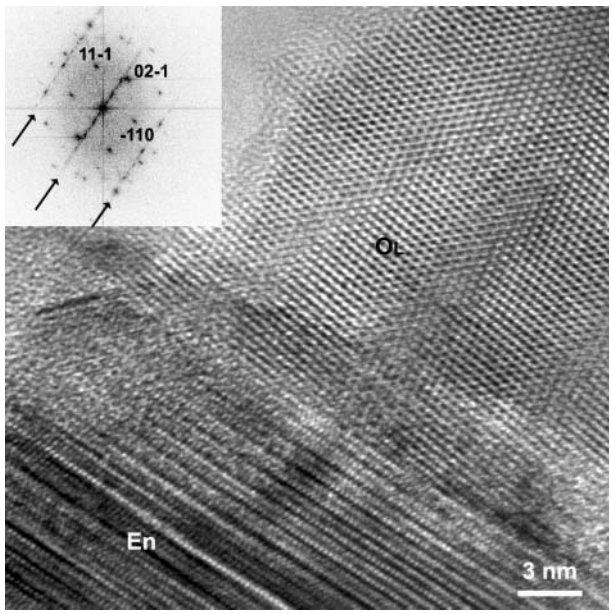

FIGURE 13. HREM image of a grain boundary between enstatite (En) and olivine (Ol). The Fourier transform (inset) shows that the olivine is oriented along [112] and the enstatite along [010]. Because enstatite has a disordered stacking along (100), its (h00) and (h0 ± 1) reflection rows are replaced by streaks (black arrows).

The TEM results presented here show small ordered domains of clinoenstatite but no topotactic relationship between the pyroxene crystals and the surrounding olivine. This finding is in agreement with earlier observations by Putnis (1979) for the oxidation of olivines from an ultrabasic layered intrusion. That author observed platelets of clinoenstatite with a completely arbitrary orientation with respect to the olivine matrix. The fact that in the present case there is not a unique, well-defined topotactic relationship between the pyroxene and forsterite crystals may indicate that many different orientations and geometric relationships are possible, including those reported by Champness (1970). For example, one of the topotactic relationships observed by Champness (1970) was $(100)_{OL} \parallel (100)_{PX}$, $\mathbf{b}_{OL} \parallel \mathbf{c}_{PX}$, $\mathbf{c}_{OL} \parallel \mathbf{b}_{PX,}$ which could be obtained by a contraction along **b** and a tilting of the tetrahedra with respect to the glide perpendicular to **a**, thus leading to the formation of the pyroxene chains (along **b** in the original forsterite setting and along **c** in the pyroxene setting). An alternative topotactic relationship and related transformation scheme not observed by Champness (1970) could be $\mathbf{a}_{OL} \parallel \mathbf{a}_{PX}$, $\mathbf{b}_{OL} \parallel \mathbf{b}_{PX}$, and $\mathbf{c}_{OL} \parallel \mathbf{c}_{PX}$ (Fig. 14), with the transformation from forsterite (Fig. 14a) to pyroxene obtained by the incorporation of Si and O, the rotation of part of the tetrahedra, and the counter diffusion of Mg atoms (Fig. 14b) leading to the formation of the pyroxene chains (Fig. 14c).

ACKNOWLEDGMENTS

This study formed part of the thesis of F. Bagatti. M. Mazzucchelli is acknowledged for providing the olivine sample. Thanks to M. Tonelli, G. Sabatino and S. Bigi for help and support during the TEM and SEM experiments. Thanks to A. Migliori (CNR-IMM) for technical assistance and useful discussions of the TEM results. N. Khisina and an anonymous referee are kindly acknowledged for their thorough review that certainly improved the quality of the manuscript.

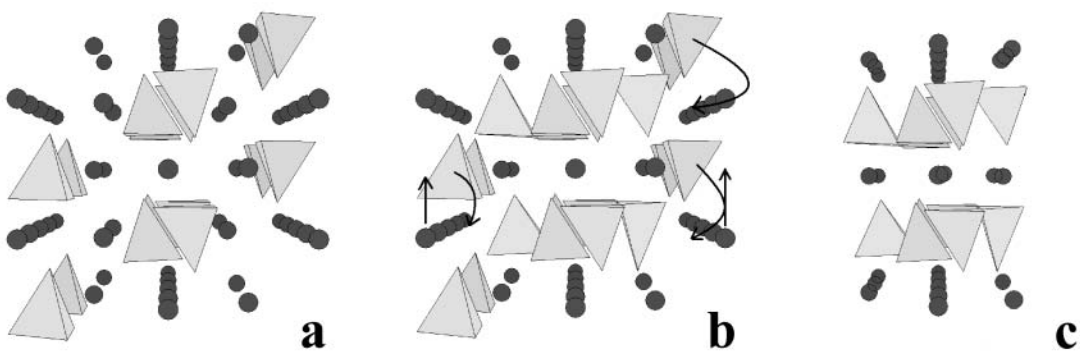

FIGURE 14. A model for the transformation from forsterite to pyroxene (**a**) in the **ab** plane of forsterite, the transformation is obtained by the incorporation of Si and O atoms, the rotation of part of the tetrahedra, and the counter diffusion of Mg atoms (**b**) leading to the formation of the pyroxene chains in the **a-b** plane (**c**).

REFERENCES CITED

Aggarwal, S., Töpfer, J., Tsai, T., and Dieckmann, R. (1997) Point defects and transport in binary and ternary, non-stoichiometric oxides. Solid State Ionics, 101–103, 321–331.

Ahra, E.H., Modaressi, A., Bessieres, J., and Heizmann, J.J. (1995) Kinetic laws for parallelepipedic samples of hematite during their topochemical reduction to magnetite. Solid State Ionics, 81, 5–14.

Artioli, G., Bellotto, M., and Palosz, B. (1993) High-temperature «in situ» Rietveld study of Fe,Mg cation partitioning in olivine. Powder Diffraction, 9, 63–67.

Bamford, C.H. and Tipper, C.F.H. (1980) Comprehensive chemical kinetics. Elsevier, New York, 22, 41–113.

Bancroft, G.M., Borne, R.G., and Maddock, A.G. (1967) Application of the Mössbauer effect to silicate mineralogy. Part 1 Iron silicates of known crystal structure. Geochimica and Cosmochimica Acta, 31, 2219–2246.

Béjina, F. and Jaoul, O. (1997) Silicon diffusion in silicate minerals. Earth and Planetary Science Letters, 153, 229–238.

Brown, G.E. (1970) The crystal chemistry of the olivines. Ph.D. Thesis, Virginia Polytechnic Institute and State University, Blacksburg, Virginia.

——— (1980) Olivines and silicate spinels. In P.H. Ribbe, Ed., Reviews in Mineralogy: Orthosilicates, 5, 275–381. Mineralogical Society of America, Washington, D.C.

Brown, G.E and Prewitt, C.T. (1973) High-temperature crystal chemistry of hortonolite. American Mineralogist, 58, 577–587.

Bush, W.R., Hafner, S.S., and Virgo, D. (1970) Some ordering of iron and magnesium at the octahedrally coordinated sites in a magnesium-rich olivine. Nature, 227, 1339–1341.

Caron, L.G., Santoro, R.P., and Newnham, R.E. (1965) Magnetic structure of $CaMnSiO_4$. Journal of Physics and Chemistry of Solids, 26, 927–930.

Chakraborty, A. (1997) Kinetics of the reduction of hematite to magnetite near its Curie transition. Journal of Magnetism and Magnetic Materials, 204, 57–60.

Champness, P.E. (1970) Nucleation and growth of iron oxides in olivines, $(Mg,Fe)_2SiO_4$. Mineralogical Magazine, 37, 790– 800.

Coats, A.W. and Redfern, J.P. (1964) Kinetic parameters from thermogravimetric data. Nature, 201, 68.

Dapiaggi, M., Artioli, G., and Petras, L. (2002) A newly developed high-temperature chamber for in situ X-ray diffraction: setup and calibration procedures. The Rigaku Journal, 19, 35–41.

Deer, W.A., Howie, R.A., and Zussmann, J. (1962) Rock-forming minerals. Vol I. Longmans.

Duke, D.A. and Stephens, J.D. (1964) Infrared investigation of the olivine group minerals. American Mineralogist, 49, 1338–1406.

Dyar, M.D., Delaney, J.S., Sutton, S.R., and Schaefer, M.W. (1998) Fe^{3+} distribution in oxidized olivine: A synchrotron micro-XANES study. American Mineralogist, 83, 1361–1365.

Finger, L.W. (1970) Fe/Mg ordering in olivines. Carnegie Institute of Washington Year Book, 67, 216–217.

Fisler, D.K., Mackwell S.J., and Petsch, S. (1997) Grain boundary diffusion in enstatite. Physics and Chemistry of Minerals, 24, 264–273.

Galwey, A.K. (1997) The low-temperature reaction of ferrous sulphide with sulphur dioxide. Thermochimica Acta, 291, 155–169.

Hazen, R.M. (1976) Effect of temperature and pressure on crystal structure of forsterite. American Mineralogist, 61, 1280–1293.

Henderson, D.W. (1979) Experimental analysis of non-isothermal transformations involving nucleation and growth. Journal of Thermal analysis, 15, 325–331.

Hovmöller, S. (1992) CRISP: crystallographic image processing on a personal computer. Ultramicroscopy, 41, 121–125.

Huggins, F.E. (1973) Cation order in olivines: evidence from vibrational spectra. Chemical Geology, 11, 99–109.

Iishi, K., Torigoe, K., and Han, X.J. (1997) Oriented precipitate complexes in iron-rich olivines produced experimentally in aqueous oxidizing environment. Physics and Chemistry of Minerals, 25, 8–14.

Ingrin, J., Pacaud, L., and Jaoul, O. (2001) Anisotropy of oxygen diffusion in diopside. Earth and Planetary Science Letters, 192, 347–361.

Janowski, J., Baranski, A., and Sadowski, A. (1996) Evolution of porosity profiles of magnetite phase during high temperature reduction of hematite. ISIJ International, 36, 269–278.

Kennedy, J.A. and Clark, S.M. (1997) A new method for the analysis of non-isothermal DSC and diffraction data. Thermochimica Acta, 307, 27–35.

Khisina, N.R., Khramov, D.A., Kolosov, M.V., Kleshev, A.A., and Taylor, L.A. (1995) Formation of ferriolivine and magnesioferrite from Mg-Fe olivine: reactions and kinetics of oxidation. Physics and Chemistry of Minerals, 22, 241–250.

Khisina, N.R., Khramov, D.A., Kleschev, A.A., and Langer, K. (1998) Laihunitization as a mechanism of olivine oxidation. European Journal of Mineralogy, 10, 229–238.

Khisina, N.R., Rusakov, V.S., and Kleshcev, A.A. (1999) Laihunite and the PO_2-T conditions of its formation. Geochemistry International, 37, 891–895.

Khisina, N.R., Langer, K., Andrut, M., Ukhanov, V., and Wirth, R. (2000) Nanoscale microstructure of Fe^{3+}-, OH^--bearing crystalline inclusions in experimentally oxidized olivine from a mantle nodule. Mineralogical Magazine, 64, 319–335.

Koltermann, M. (1962) Der Thermische Zerfall faylalithaltinger Olivine bai hohen Temperaturen. Neues Jahrbuch Mineralogie Monatshelfte, 181–191.

Kondoh, S., Kitamura, M., and Morimoto, N. (1985) Synthetic laihunite ($\square_x Fe^{2+}_{2-3x}Fe^{3+}_{2x}SiO_4$), an oxydation product of olivine. American Mineralogist, 70, 737–746.

Larson, A.C. and Von Dreele, R.B. (1994). GSAS manual, Los Alamos National Laboratory Report LAUR 86–748.

MacKenzie, K.J.D. and Meinhold, R.H. (1994) Thermal reactions of chrysotile revisited: a ^{29}Si and ^{25}Mg MAS NMR study. American Mineralogist, 79, 43–50.

Mackwell, S.I. (1992) Oxidation kinetics of fayalite (Fe_2SiO_4). Physics and Chemistry of Minerals, 19, 220–228.

Malek, J. and Mitsuhashi, T. (2000) Testing method for the Johnson-Mehl-Avrami equation in kinetic analysis of crystallization processes. Journal of American Ceramic Society, 83, 2103–2105.

Mikouchi, T., Yamada, I., and Miyamoto, M. (2000) Symplectic exsolution in olivine from the Nakhla martian meteorite. Meteoritics and Planetary Science, 35, 937–942.

Moseley, D. (1984) Symplectite exsolution in olivine. American Mineralogist, 69, 139–153.

Murray, P. and White, J. (1955) Kinetics of thermal dehydration characteristics of clay minerals I. Transaction British Ceramic Society, 54, 137–150.

Newnham, R.E., Caron, L.G., and Santoro, R.P. (1966) Magnetic properties of $CaCoSiO_4$ and $CaFeSiO_4$. Journal of American Ceramic Society, 49, 284–285.

Nobuyuki, A., Mineo, K., and Masayasu, T. (1985) Temperature dependence of intersite distribution of Mg and Fe in olivine and associated change of lattice parameters. Physics and Chemistry of Minerals, 12, 1–10.

Ottonello, G., Princivalle, F., and Della Giusta, A. (1990) Temperature, composition and f_{O2} effects on intersite distribution of Mg and Fe^{2+} in olivines. Physics and Chemistry of Minerals, 17, 301–312.

Princivalle, F. (1990) Influence of temperature and composition on Mg-Fe^{2+} intracrystalline distribution of olivines. Mineralogy and Petrology, 43, 121–129.

Puga, E., Cruz, M.D.R., and De Federico, A.D. (1999) Magnetite-silicate inclusions in olivine of ophiolitic metagabbros from the Mulhacén Complex, Betic Cordillera, southeastern Spain. The Canadian Mineralogist, 37, 1191–1209.

Putnis, A. (1979) Elecron microscopy and petrography of hig temperature oxidation in olivine from Rhum layered intrusion. Mineralogical Magazine, 43, 293–296.

Putnis, A. and McConnell, J.D.C. (1980) Principles of mineral behaviour. Elsevier, New York.

Redfern, S.A.T., Henderson, C.M.B., Knight, K.S., and Wood, B.J. (1997) High-temperature order-disorder in $(Fe_{0.5}Mn_{0.5})_2SiO_4$ and $(Mg_{0.5}Mn_{0.5})_2SiO_4$ olivines: an «in situ» neutron diffraction study. European Journal of Mineralogy, 9, 287–300.

Rivalenti, G., Rossi, A., Siena, F., and Sinogoi, S. (1984) The layered Series of the Ivre-Verbano Igneous Complex, Western Alps, Italy. Tschermaks Mineralogie and Petrologie Mitteilungen, 33, 77–99.

Scheetz, B.E. and White, W.B. (1972) Synthesis and optical absorption spectra of Cr^{2+}-containing orthosilicates. Contribution to Mineralogy and Petrology, 37, 221–227.

Smyth, J.R. and Hazen, R.M. (1973) The crystal structure of forsterite and hortonolite at several temperature up to 900°C. American Mineralogist, 58, 588–593.

Treiman, A.H. (1998) The history of Allen Hills 84001 revised: multiple shock events. Meteorite and Planetary Science, 33, 753–764.

Veblen, D.R. (1991) Polysomatism and polysomatic series: a review and applications. American Mineralogist, 76, 801–826.

Weeks, R.A., Pigg, J.C., and Finch, C.B. (1974) Charge-transfer spectra of Fe^{3+} and Mg^{2+} in synthetic forsterite (Mg_2SiO_4). American Mineralogist, 59, 1259–1266.

Will, G. and Nover, G. (1979) Influence of oxigen partial pressure on the Mg/Fe distribution in olivines. Physics and Chemistry of Minerals, 4, 199–208.

Wood, B.J. (1974) Crystal field spectrum of Ni^{2+} in olivine. American Mineralogist, 59, 244–248.

Wu, T. and Kohlstedt, D.L. (1988) Rutherford backscattering spectroscopy study of $(Mg, Fe)_2SiO_4$. Journal of American Ceramic Society, 71, 540–545.

MANUSCRIPT RECEIVED JANUARY 14, 2003
MANUSCRIPT ACCEPTED MAY 30, 2003
MANUSCRIPT HANDLED BY DARBY DYAR